

## Article

# Solidification Behavior of Dy-Tb-Fe Alloys through Experimental Study and Thermodynamic Calculation

Cong Tan <sup>1</sup>, Qi Wei <sup>1</sup>, Weifeng Cheng <sup>1</sup>, Xingyu Liu <sup>1</sup>, Yuchen Bai <sup>1</sup> and Jiang Wang <sup>1,2,\*</sup> 

<sup>1</sup> Guangxi Key Laboratory of Information Materials, School of Materials Science and Engineering, Guilin University of Electronic Technology, Guilin 541004, China; tancong0526@163.com (C.T.); 17773055566@163.com (Q.W.); m17828906669@163.com (W.C.); liuxingyu0026@163.com (X.L.); 13124132992@163.com (Y.B.)

<sup>2</sup> Engineering Research Center of Electronic Information Materials and Devices, Ministry of Education, Guilin University of Electronic Technology, Guilin 541004, China

\* Correspondence: waj124@guet.edu.cn

**Abstract:** In this work, the solidification microstructure and phase transitions of Dy-Tb-Fe alloy samples were studied by using scanning electron microscopy with energy dispersive spectroscopy (SEM-EDS), X-ray diffraction (XRD) and differential thermal analysis (DTA). No stable ternary compound was detected in the present experiments. The phase transformation temperatures of eight Dy-Tb-Fe alloy samples were measured. Based on the experimental results determined in this work and reported in the literature, the phase equilibria of the Dy-Tb-Fe system was calculated using the CALPHAD method. The calculated vertical sections are consistent with the experimental results determined in this work and reported in the literature. Furthermore, in combination with the experimental solidification microstructure, the solidification behavior of Dy-Tb-Fe alloy samples was analyzed through the thermodynamic calculation with the Gulliver–Scheil non-equilibrium model. The simulated results agree well with the experimental results. This indicates that the reasonable thermodynamic parameters of the Dy-Tb-Fe system were finally obtained.

**Keywords:** Dy-Tb-Fe; solidification microstructure; phase transition; thermodynamic calculation



**Citation:** Tan, C.; Wei, Q.; Cheng, W.; Liu, X.; Bai, Y.; Wang, J. Solidification Behavior of Dy-Tb-Fe Alloys through Experimental Study and Thermodynamic Calculation. *Materials* **2023**, *16*, 4697. <https://doi.org/10.3390/ma16134697>

Academic Editor: Elena Pereloma

Received: 3 June 2023

Revised: 24 June 2023

Accepted: 27 June 2023

Published: 29 June 2023



**Copyright:** © 2023 by the authors. Licensee MDPI, Basel, Switzerland. This article is an open access article distributed under the terms and conditions of the Creative Commons Attribution (CC BY) license (<https://creativecommons.org/licenses/by/4.0/>).

## 1. Introduction

Nd-Fe-B permanent magnets with excellent magnetic properties have been widely used in various industrial fields such as wind turbines, electric vehicles, and aerospace [1–5]. With the increase in the operation temperature, the magnetic properties (e.g., coercivity and remanence) of Nd-Fe-B permanent magnets decrease [6–9]. In order to ensure the sufficient coercivity of Nd-Fe-B permanent magnets at the operation temperature, the addition of heavy rare earth elements (Dy, Tb, etc.) to Nd-Fe-B permanent magnets to partially substitute Nd is an effective method because the magnetocrystalline anisotropy fields of Dy<sub>2</sub>Fe<sub>14</sub>B and Tb<sub>2</sub>Fe<sub>14</sub>B are much higher than that of Nd<sub>2</sub>Fe<sub>14</sub>B, which would result in the great improvement of the coercivity for the permanent magnets [10–12]. To reduce the content of heavy rare earth metals Dy and Tb in Nd-Fe-B permanent magnets, the grain boundary diffusion process (GBDP) was developed recently [13]. During the GBDP, first, Dy and Tb can diffuse along the grain boundary phase into the interior of the magnet; then, the partial Nd on the surface of Nd<sub>2</sub>Fe<sub>14</sub>B grains is replaced by Dy and Tb to form a core–shell microstructure containing Nd<sub>2</sub>Fe<sub>14</sub>B and (Dy, Tb)<sub>2</sub>Fe<sub>14</sub>B. The substitution of Nd by Dy and Tb dilutes the ferromagnetism of the grain boundary phase and further weakens the coupling between neighboring grains, which enhances the coercivity of the magnets after the grain boundary diffusion process [14,15]. In order to gain a deeper understanding of the grain boundary diffusion process, the thermodynamics and kinetics of Nd-Fe-B permanent magnets containing Tb and Dy elements are fundamental to enhance the overall performance of Nd-Fe-B magnets [16]. In particular, the solidification process

of Nd-Fe-B-based alloys is significantly important to control microstructure and improve magnetic properties of Nd-Fe-B permanent magnets [17]. Solidification is a process in which the liquid phase decreases gradually and the solid phase is formed by peritectic, eutectic and other reactions during the cooling process until the liquid phase disappears completely [18]. Using thermodynamic calculations, the Scheil–Gulliver model can be employed to simulate the non-equilibrium solidification process of as-cast alloys [19]. In our previous work, the RE-Fe (RE = Pr, Nd, Sm, Gd, Dy, Tb, Ho, Tm, Lu, Y) [20–24], RE-B (RE = La, Ce, Pr, Nd, Sm, Gd, Dy, Tb, Ho, Tm, Lu, Y) [25–27], and RE<sub>1</sub>-RE<sub>2</sub> binary systems [28] were calculated, and then thermodynamic calculations of the RE<sub>1</sub>-RE<sub>2</sub>-Fe (e.g., La-Ce-Fe and Ce-Nd-Fe [29], La-Pr-Fe and Ce-Pr-Fe [30]) ternary systems and the Nd-Fe-B ternary system [31] were performed. Furthermore, the development of a thermodynamic database of Nd-Dy-Tb-Fe-B magnets is in progress in our group.

In this work, the solidification microstructure and phase transitions of Dy-Tb-Fe as-cast alloy samples were investigated experimentally, and then phase equilibria of this ternary system was calculated using the CALPHAD method. Finally, the solidification behaviors of Dy-Tb-Fe as-cast alloy samples were investigated using the Scheil–Gulliver non-equilibrium model. It could demonstrate a solid foundation for the microstructure design of high-performance Nd-Fe-B permanent magnet materials with Dy and Tb elements.

## 2. Literature Information

### 2.1. Binary Systems

The thermodynamic database of Dy-Fe and Tb-Fe systems in the high-temperature range (above 800 K) was established by Landin et al. [32], but the contribution of magnetism to the Gibbs energy and experimental heat capacity of all intermetallic compounds were not taken into account. Rong et al. [22] optimized the Dy-Fe and Tb-Fe systems using the CALPHAD method considering the magnetic contribution and experimental heat capacity of the intermetallic compounds. The calculation results including phase relationship and thermodynamic properties are in good agreement with the experimental results. Recently, Ye et al. [24] re-conducted thermodynamic calculations for Dy-Fe and Tb-Fe systems to achieve compatibility with the RE-Fe thermodynamic database. The results of the Dy-Fe and Tb-Fe systems optimized by Ye et al. [24] were used in the present calculation of the Dy-Tb-Fe system.

The Dy-Tb phase diagram was not calculated in the reported literature up to now. Gschneidner et al. [33,34] reported that Dy and Tb are completely miscible and measured lattice parameters of the Dy-Tb alloys in the systematic review of lanthanide binary systems. According to the reported data [33,34], the Dy-Tb phase diagram was drawn by Moffatt [35] considering the continuous solid solution phases formed from  $\beta$ -Dy,  $\beta$ -Tb,  $\alpha$ -Dy and  $\alpha$ -Tb phases due to their same crystal structures [36]. Therefore, all the phases including liquid phase, bcc ( $\beta$ -Dy,  $\beta$ -Tb) and hcp ( $\alpha$ -Dy,  $\alpha$ -Tb) in the Dy-Tb system were described by using the ideal solution model. Figure 1 shows the calculated Dy-Tb phase diagram in this work.

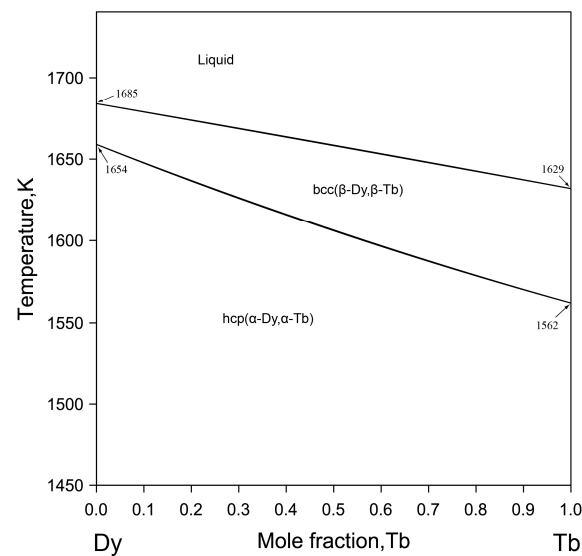


**Figure 1.** The calculated Dy-Tb binary phase diagram in this work.

## 2.2. Ternary System

The Dy<sub>0.73</sub>Tb<sub>0.27</sub>-Fe vertical section of the Dy-Tb-Fe system was measured by Westwood et al. [37] with DTA, X-ray diffraction and metallography. Landin et al. [32] directly extrapolated the Dy-Tb-Fe system based on the experimental results of Westwood et al. and Abell et al. [38], including the Dy<sub>0.73</sub>Tb<sub>0.27</sub>-Fe vertical section and liquidus projection. Although the values of the calculated Dy<sub>0.73</sub>Tb<sub>0.27</sub>-Fe vertical section are consistent with the experimental data [37], Ye et al. [24] have recently reassessed the calculations of the Dy-Fe and Tb-Fe systems. Therefore, thermodynamic calculations for the Dy-Tb-Fe system are still necessary.

## 3. Experimental Procedure

Eight Dy-Tb-Fe alloy samples with compositions of  $x_{Dy} : x_{Tb} = 1 : 1$  were prepared from bulk Dy, Tb and Fe (99.99% purity, China New Metal Material Technology Company, Ltd., Beijing, China). Each alloy sample (about 4 g) was melted 3–5 times in a vacuum arc melting furnace filled with argon gas to ensure uniform composition. The alloy samples were cooled in a copper crucible with cooling water, and thus the solidification process of the alloy samples was non-equilibrium due to the fast cooling rate.

The as-cast alloy samples were prepared by standard metallographic procedure. The morphology and phase composition of the alloy samples were measured by scanning electron microscope with energy dispersive spectroscopy (SEM-EDS, FEI 450G, FEI Company, Hillsboro, OR, USA). The compositions of each phase in the alloy samples were measured four times by EDS, and the standard deviations of the measured composition data were determined. After the alloy sample was ground into powder in anhydrous ethanol, the phase structures of the formed phases in the alloy samples were analyzed by X-ray powder diffraction (XRD, PLXcel 3D, Cu K<sub>α</sub> radiation). The phase transition temperatures of the alloy samples were measured by differential thermal analysis (DTA, TA Instruments SDT/Q-600) using high-purity Al<sub>2</sub>O<sub>3</sub> crucibles in a flowing argon atmosphere. Considering that rare earth metals are prone to oxidation, a heating/cooling rate of 20 K/min was used in DTA measurement.

## 4. Thermodynamic Calculation

### 4.1. Solution Phases

The solution phase  $\varphi$  including liquid, fcc, bcc and hcp is described by using the substitutional solution model. The molar Gibbs energy of the solution phase  $\varphi$  can be expressed as follows:

$$G_m^\varphi = \sum_{i=Dy,Tb,Fe} x_i {}^0G_i^\varphi + RT \sum_{i=Dy,Tb,Fe} x_i \ln x_i + {}^{mag}G_m^\varphi + {}^{ex}G_m^\varphi, \quad (1)$$

$$\begin{aligned} {}^{ex}G_m^\varphi = & x_{Dy}x_{Tb} \sum_{j=0}^j L_{Dy,Tb}^\varphi (x_{Dy}-x_{Tb})^j + x_{Dy}x_{Fe} \sum_{j=0}^j L_{Dy,Fe}^\varphi (x_{Dy}-x_{Fe})^j, \\ & + x_{Tb}x_{Fe} \sum_{j=0}^j L_{Tb,Fe}^\varphi (x_{Tb}-x_{Fe})^j + x_{Dy}x_{Tb}x_{Fe} L_{Dy,Tb,Fe}^\varphi, \end{aligned} \quad (2)$$

$${}^{mag}G_m^\varphi = RT \ln(\beta_0 + 1)g(\tau), \quad (3)$$

$$L_{Dy,Tb,Fe}^\varphi = x_{Dy} {}^0L_{Dy,Tb,Fe}^\varphi + x_{Tb} {}^1L_{Dy,Tb,Fe}^\varphi + x_{Fe} {}^2L_{Dy,Tb,Fe}^\varphi, \quad (4)$$

where  $x_i$  is the mole fraction of element  $i$  ( $i = Dy, Tb, Fe$ ) and  ${}^0G_i^\varphi$  means the molar Gibbs energy of phase  $\varphi$  for element  $i$  ( $i = Dy, Tb, Fe$ ); these values refer to the SGTE database [39].  $R$  is the gas constant and  $T$  is the absolute temperature (Kelvin).  ${}^{mag}G_m^\varphi$  is the magnetic contribution to Gibbs energy of the magnetic phase. In Equation (3),  $\tau = T/T_c^\varphi$ , and  $T_c^\varphi$  is the Curie temperature of the phase  $\varphi$ .  $\beta_0$  is the Bohr magnetons.  ${}^jL_{Dy,Fe}^\varphi$  and  ${}^jL_{Tb,Fe}^\varphi$  are the interaction parameters and are taken from the Dy-Fe and Tb-Fe systems evaluated by Ye et al. [24], respectively.  ${}^0L_{Dy,Tb,Fe}^\varphi$ ,  ${}^1L_{Dy,Tb,Fe}^\varphi$  and  ${}^2L_{Dy,Tb,Fe}^\varphi$  are the ternary interaction parameters to be evaluated.

### 4.2. Intermetallic Compounds

In the Dy-Tb-Fe system, a continuous solid solution is formed because of the same crystal structure of DyFe<sub>2</sub> and TbFe<sub>2</sub> [40–42]. Similarly, DyFe<sub>3</sub> and TbFe<sub>3</sub>, Dy<sub>6</sub>Fe<sub>23</sub> and Tb<sub>6</sub>Fe<sub>23</sub>, Dy<sub>2</sub>Fe<sub>17</sub> and Tb<sub>2</sub>Fe<sub>17</sub> also form a continuous solid solution in the Dy-Tb-Fe system. Therefore, these intermetallic compounds are modeled by (Dy, Tb)<sub>0.3333</sub>Fe<sub>0.6667</sub>, (Dy, Tb)<sub>0.25</sub>Fe<sub>0.75</sub>, (Dy, Tb)<sub>0.2069</sub>Fe<sub>0.7931</sub> and (Dy, Tb)<sub>0.1053</sub>Fe<sub>0.8947</sub>, which are named REFe<sub>2</sub>, REFe<sub>3</sub>, RE<sub>6</sub>Fe<sub>23</sub> and RE<sub>2</sub>Fe<sub>17</sub> (RE = Dy, Tb). Their molar Gibbs energies can be expressed as

$$\begin{aligned} G_m^{REFe_2} = & Y_{Dy} G_{Dy:Fe}^{REFe_2} + Y_{Tb} G_{Tb:Fe}^{REFe_2} + 0.3333RT (Y_{Dy} \ln Y_{Dy} + Y_{Tb} \ln Y_{Tb}) \\ & + Y_{Dy} Y_{Tb} {}^jL_{Dy,Tb:Fe}^{REFe_2} (x_{Dy}-x_{Tb})^j + {}^{mag}G_m^{REFe_2}, \end{aligned} \quad (5)$$

$${}^jL_{Dy,Tb:Fe}^{REFe_2} = A_1 + B_1T, \quad (6)$$

$$\begin{aligned} G_m^{REFe_3} = & Y_{Dy} G_{Dy:Fe}^{REFe_3} + Y_{Tb} G_{Tb:Fe}^{REFe_3} + 0.25RT (Y_{Dy} \ln Y_{Dy} + Y_{Tb} \ln Y_{Tb}) \\ & + Y_{Dy} Y_{Tb} {}^jL_{Dy,Tb:Fe}^{REFe_3} (x_{Dy}-x_{Tb})^j + {}^{mag}G_m^{REFe_3}, \end{aligned} \quad (7)$$

$${}^jL_{Dy,Tb:Fe}^{REFe_3} = A_2 + B_2T, \quad (8)$$

$$\begin{aligned} G_m^{RE_6Fe_{23}} = & Y_{Dy} G_{Dy:Fe}^{RE_6Fe_{23}} + Y_{Tb} G_{Tb:Fe}^{RE_6Fe_{23}} + 0.2069RT (Y_{Dy} \ln Y_{Dy} + Y_{Tb} \ln Y_{Tb}) \\ & + Y_{Dy} Y_{Tb} {}^jL_{Dy,Tb:Fe}^{RE_6Fe_{23}} (x_{Dy}-x_{Tb})^j + {}^{mag}G_m^{RE_6Fe_{23}}, \end{aligned} \quad (9)$$

$${}^jL_{Dy,Tb:Fe}^{RE_6Fe_{23}} = A_3 + B_3T, \quad (10)$$

$$G_m^{RE_2Fe_{17}} = Y_{Dy} G_{Dy:Fe}^{RE_2Fe_{17}} + Y_{Tb} G_{Tb:Fe}^{RE_2Fe_{17}} + 0.1053RT (Y_{Dy} \ln Y_{Dy} + Y_{Tb} \ln Y_{Tb}) + Y_{Dy} Y_{Tb} j_{Dy,Tb:Fe}^{RE_2Fe_{17}} (x_{Dy} - x_{Tb})^j + {}^{mag} G_m^{RE_2Fe_{17}}, \quad (11)$$

$$j_{Dy,Tb:Fe}^{RE_2Fe_{17}} = A_4 + B_4 T, \quad (12)$$

in which  $j_{Dy:Fe}^{REFe_2}$ ,  $j_{Tb:Fe}^{REFe_2}$ ,  $j_{Dy:Fe}^{REFe_3}$ ,  $j_{Tb:Fe}^{REFe_3}$ ,  $j_{Dy:Fe}^{RE_6Fe_{23}}$ ,  $j_{Tb:Fe}^{RE_6Fe_{23}}$ ,  $j_{Dy:Fe}^{RE_2Fe_{17}}$  and  $j_{Tb:Fe}^{RE_2Fe_{17}}$  are interaction parameters taken from the Dy-Fe and Tb-Fe systems assessed by Ye et al. [24].  $j_{Dy,Tb:Fe}^{REFe_2}$ ,  $j_{Dy,Tb:Fe}^{REFe_3}$ ,  $j_{Dy,Tb:Fe}^{RE_6Fe_{23}}$  and  $j_{Dy,Tb:Fe}^{RE_2Fe_{17}}$  are the interaction parameters to be optimized.

## 5. Results and Discussion

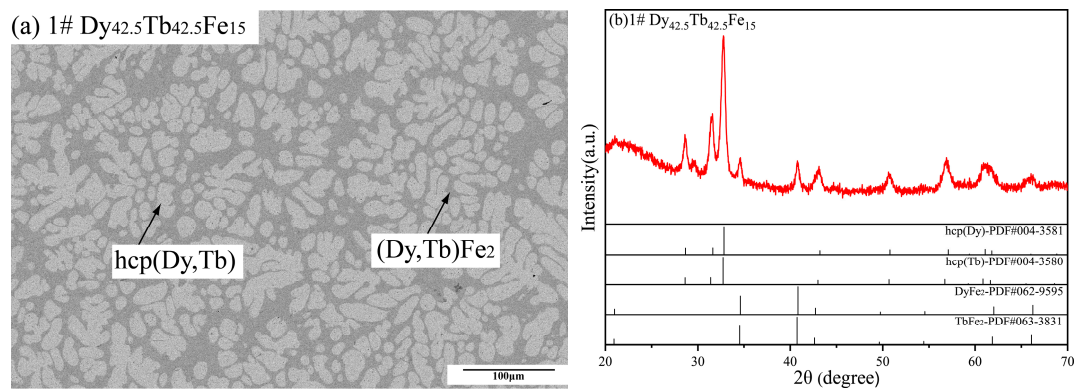
The microstructure and phase transitions of eight Dy-Tb-Fe as-cast alloy samples were determined in this work. The phase compositions and phase transition temperatures of the alloy samples measured by EDS, XRD and DTA are shown in Table 1.

**Table 1.** Phase compositions and identified phases of Dy-Tb-Fe alloy samples.

Nominal Composition (at.%)	SEM-EDS Results (at.%)			Identified Phases by EDS and XRD	Phase Transitions (K)	Solidification Process
	Dy	Tb	Fe			
1#-Dy <sub>42.5</sub> Tb <sub>42.5</sub> Fe <sub>15</sub>	46.77 ± 0.2	47.74 ± 0.6	5.49 ± 0.4	hcp (Dy, Tb) (Dy, Tb) Fe <sub>2</sub>	1030, 1057, 1435	L → hcp (Dy, Tb) L → hcp (Dy, Tb) + (Dy, Tb) Fe <sub>2</sub>
	17.88 ± 0.6	13.91 ± 0.2	68.21 ± 0.4			
2#-Dy <sub>25</sub> Tb <sub>25</sub> Fe <sub>50</sub>	17.51 ± 0.7	15.46 ± 0.3	67.03 ± 0.6	(Dy, Tb) Fe <sub>2</sub> hcp (Dy, Tb)	1121, 1131, 1459	L → (Dy, Tb) Fe <sub>2</sub> L → hcp (Dy, Tb) + (Dy, Tb) Fe <sub>2</sub>
	40.64 ± 0.2	52.09 ± 0.1	7.27 ± 0.2			
3#-Dy <sub>20</sub> Tb <sub>20</sub> Fe <sub>60</sub>	17.33 ± 0.7	15.96 ± 0.1	66.71 ± 0.8	(Dy, Tb) Fe <sub>2</sub> hcp (Dy, Tb)	1490	
	37.29 ± 0.4	55.31 ± 0.8	7.40 ± 1.0			
4#-Dy <sub>15</sub> Tb <sub>15</sub> Fe <sub>70</sub>	11.45 ± 0.6	11.81 ± 0.5	76.74 ± 0.6	(Dy, Tb) Fe <sub>3</sub> (Dy, Tb) Fe <sub>2</sub>	1494, 1501	L → (Dy, Tb) Fe <sub>3</sub> L → (Dy, Tb) Fe <sub>2</sub> + (Dy, Tb) Fe <sub>3</sub>
	14.57 ± 0.1	17.95 ± 0.1	67.48 ± 0.1			
5#-Dy <sub>13.5</sub> Tb <sub>13.5</sub> Fe <sub>73</sub>	10.34 ± 0.3	12.91 ± 0.2	76.75 ± 0.1	(Dy, Tb) Fe <sub>3</sub> (Dy, Tb) Fe <sub>2</sub>	1475, 1505	
	13.07 ± 0.3	17.41 ± 0.3	69.52 ± 0.6			
6#-Dy <sub>12</sub> Tb <sub>12</sub> Fe <sub>76</sub>	3.96 ± 0.3	6.37 ± 0.5	89.67 ± 0.4	(Dy, Tb) <sub>2</sub> Fe <sub>17</sub> (Dy, Tb) <sub>6</sub> Fe <sub>23</sub> (Dy, Tb) Fe <sub>3</sub>	1482, 1495, 1555	L → (Dy, Tb) <sub>6</sub> Fe <sub>23</sub> L → (Dy, Tb) Fe <sub>3</sub> + (Dy, Tb) <sub>6</sub> Fe <sub>23</sub>
	9.05 ± 0.1	11.73 ± 0.3	79.22 ± 0.3			
	11.01 ± 0.2	12.95 ± 0.3	76.04 ± 0.4			
7#-Dy <sub>10.5</sub> Tb <sub>10.5</sub> Fe <sub>79</sub>	3.54 ± 0.1	6.16 ± 0.5	90.30 ± 0.4	(Dy, Tb) <sub>2</sub> Fe <sub>17</sub> (Dy, Tb) <sub>6</sub> Fe <sub>23</sub> (Dy, Tb) Fe <sub>3</sub>	1497, 1562	
	9.14 ± 0.1	11.48 ± 0.2	79.38 ± 0.2			
	10.10 ± 0.2	13.33 ± 0.2	76.57 ± 0.4			
8#-Dy <sub>9</sub> Tb <sub>9</sub> Fe <sub>82</sub>	3.54 ± 0.1	5.18 ± 0.3	91.28 ± 0.4	(Dy, Tb) <sub>2</sub> Fe <sub>17</sub> (Dy, Tb) <sub>6</sub> Fe <sub>23</sub>	1523, 1560	L → (Dy, Tb) <sub>2</sub> Fe <sub>17</sub> L → (Dy, Tb) <sub>2</sub> Fe <sub>17</sub> + (Dy, Tb) <sub>6</sub> Fe <sub>23</sub>
	10.21 ± 0.1	11.87 ± 0.4	77.92 ± 0.5			

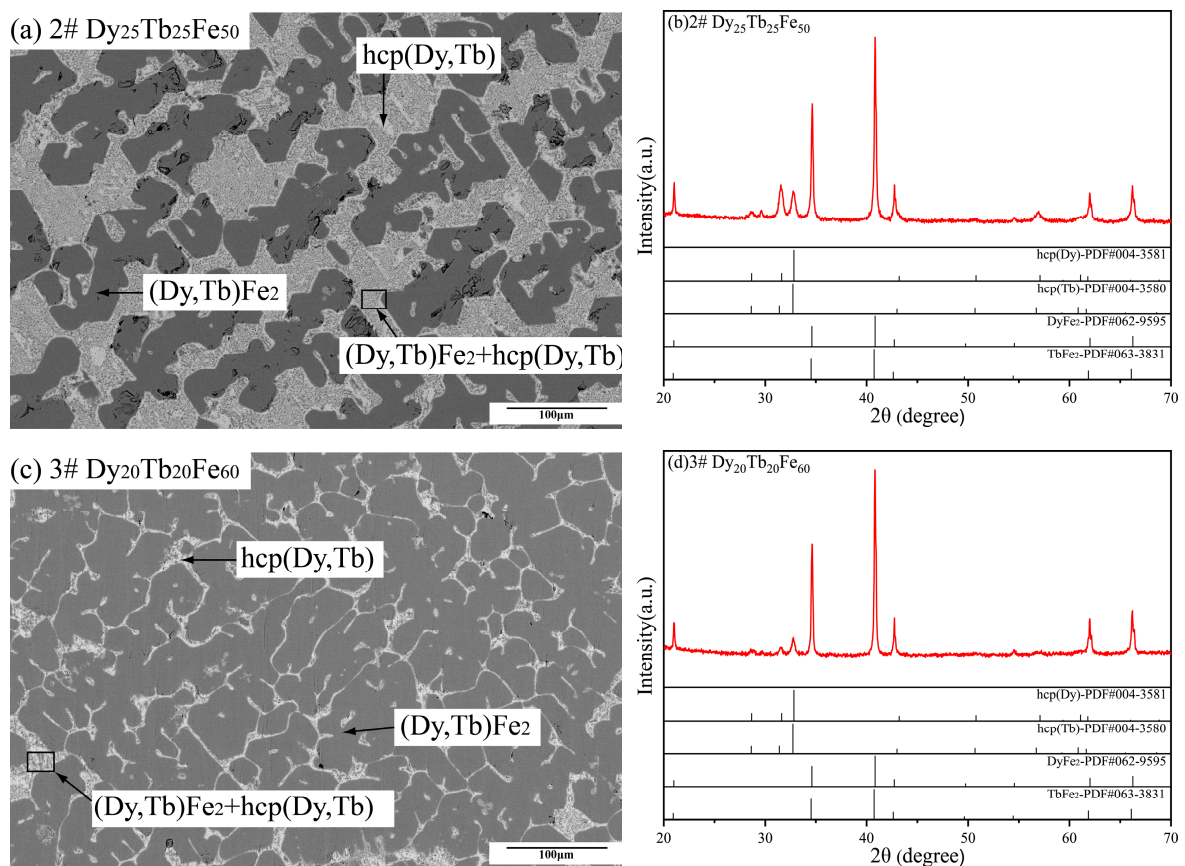
### 5.1. Solidification Microstructure

Figure 2 contains the BSE micrograph and XRD patterns of Dy<sub>42.5</sub>Tb<sub>42.5</sub>Fe<sub>15</sub> alloy sample. In Figure 2a, the microstructure of this sample shows the formation of two phases, and the composition of the gray phase was measured by EDS to be 17.88 at.% Dy, 13.91 at.% Tb and 68.21 at.% Fe, while that of the light gray phase was determined to be 46.77 at.% Dy, 47.74 at.% Tb and 5.49 at.% Fe. According to the results determined by EDS in Table 1, the gray phase and the light gray phase were identified to be (Dy, Tb) Fe<sub>2</sub> and hcp (Dy, Tb), respectively, which was same as those of the XRD patterns in Figure 2b. Moreover, there is a large amount of the hcp (Dy, Tb) phase in Figure 2b, and the background of the diffraction pattern is too high and the spectral peak is not smooth, which is the result of the internal stress or preferred orientation generated during the preparation of metal powders. In addition, the microstructure characteristics of the Dy<sub>42.5</sub>Tb<sub>42.5</sub>Fe<sub>15</sub> alloy sample indicate that the light gray hcp (Dy, Tb) phase was formed first from the liquid phase during the solidification process.



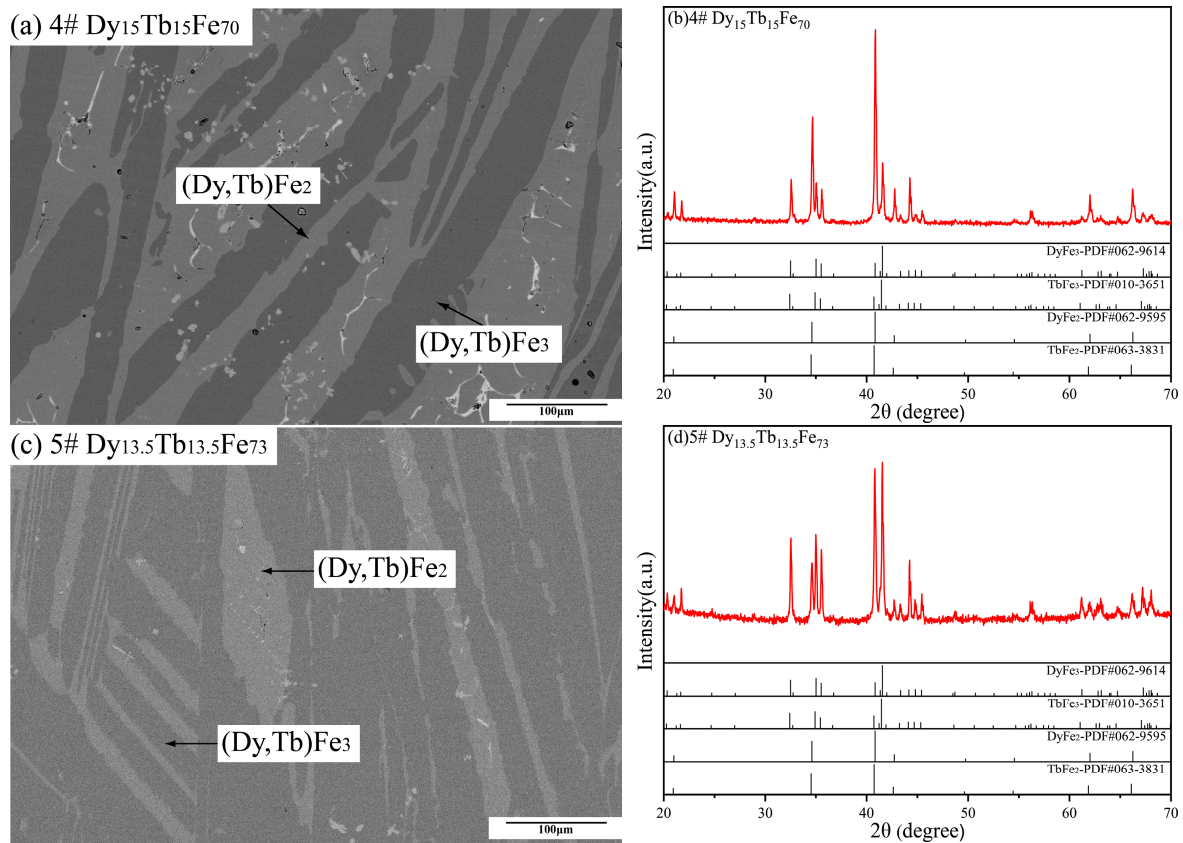
**Figure 2.** (a) Back-scattered electron (BSE) micrograph and (b) XRD patterns of  $\text{Dy}_{42.5}\text{Tb}_{42.5}\text{Fe}_{15}$  as-cast alloy sample.

Figure 3 shows the BSE and XRD images of  $\text{Dy}_{25}\text{Tb}_{25}\text{Fe}_{50}$  and  $\text{Dy}_{20}\text{Tb}_{20}\text{Fe}_{60}$  alloy samples. In Figure 3a,c,  $\text{Dy}_{25}\text{Tb}_{25}\text{Fe}_{50}$  and  $\text{Dy}_{20}\text{Tb}_{20}\text{Fe}_{60}$  alloy samples are composed of two phases, while their XRD patterns demonstrate the formation of the  $(\text{Dy, Tb})\text{Fe}_2$  and  $\text{hcp}(\text{Dy, Tb})$  phase in Figure 3b,d. According to EDS results, there are two phases present in these two samples, with  $(\text{Dy, Tb})\text{Fe}_2$  in dark gray and  $\text{hcp}(\text{Dy, Tb})$  in light gray. It means that the SEM-EDS results of these two samples are consistent with their XRD results. Meanwhile, the formation of the primary phase  $(\text{Dy, Tb})\text{Fe}_2$  and similar eutectic microstructure including  $(\text{Dy, Tb})\text{Fe}_2$  and  $\text{hcp}(\text{Dy, Tb})$  was observed from the BSE micrographs of these two as-cast alloy samples.



**Figure 3.** Back-scattered electron (BSE) micrographs and XRD patterns of  $\text{Dy}_{25}\text{Tb}_{25}\text{Fe}_{50}$  and  $\text{Dy}_{20}\text{Tb}_{20}\text{Fe}_{60}$  as-cast alloy samples. (a,b)  $\text{Dy}_{25}\text{Tb}_{25}\text{Fe}_{50}$ , (c,d)  $\text{Dy}_{20}\text{Tb}_{20}\text{Fe}_{60}$ .

As shown in Figure 4a,c,  $\text{Dy}_{15}\text{Tb}_{15}\text{Fe}_{70}$  and  $\text{Dy}_{13.5}\text{Tb}_{13.5}\text{Fe}_{73}$  alloy samples present the microstructure of two phases. Based on the composition measurements in Table 1, these two phases are identified to be  $(\text{Dy, Tb})\text{Fe}_2$  and  $(\text{Dy, Tb})\text{Fe}_3$ , which are in good agreement with the XRD patterns in Figure 4b,d. Similarly, the microstructure characteristics of  $\text{Dy}_{15}\text{Tb}_{15}\text{Fe}_{70}$  and  $\text{Dy}_{13.5}\text{Tb}_{13.5}\text{Fe}_{73}$  alloy samples show that the  $(\text{Dy, Tb})\text{Fe}_3$  phase is the primary phase during this solidification process.



**Figure 4.** Back-scattered electron (BSE) micrographs and XRD patterns of  $\text{Dy}_{15}\text{Tb}_{15}\text{Fe}_{70}$  and  $\text{Dy}_{13.5}\text{Tb}_{13.5}\text{Fe}_{73}$  as-cast alloy samples. (a,b)  $\text{Dy}_{15}\text{Tb}_{15}\text{Fe}_{70}$ , (c,d)  $\text{Dy}_{13.5}\text{Tb}_{13.5}\text{Fe}_{73}$ .

Figure 5 displays the BSE micrographs and XRD patterns of  $\text{Dy}_{12}\text{Tb}_{12}\text{Fe}_{76}$  and  $\text{Dy}_{10.5}\text{Tb}_{10.5}\text{Fe}_{79}$  alloy samples. In Figure 5a,c, three different phases were formed in these two samples. As given in Table 1, the experimental results obtained by EDS indicate that the light gray phase, the gray phase, and the dark black phase are  $(\text{Dy, Tb})\text{Fe}_3$ ,  $(\text{Dy, Tb})_6\text{Fe}_{23}$  and  $(\text{Dy, Tb})_2\text{Fe}_{17}$ , respectively, which are same as those of the XRD patterns in Figure 5b,d. The microstructures of  $\text{Dy}_{12}\text{Tb}_{12}\text{Fe}_{76}$  and  $\text{Dy}_{10.5}\text{Tb}_{10.5}\text{Fe}_{79}$  alloy samples suggest that the  $(\text{Dy, Tb})_6\text{Fe}_{23}$  phase as the primary phase was formed.

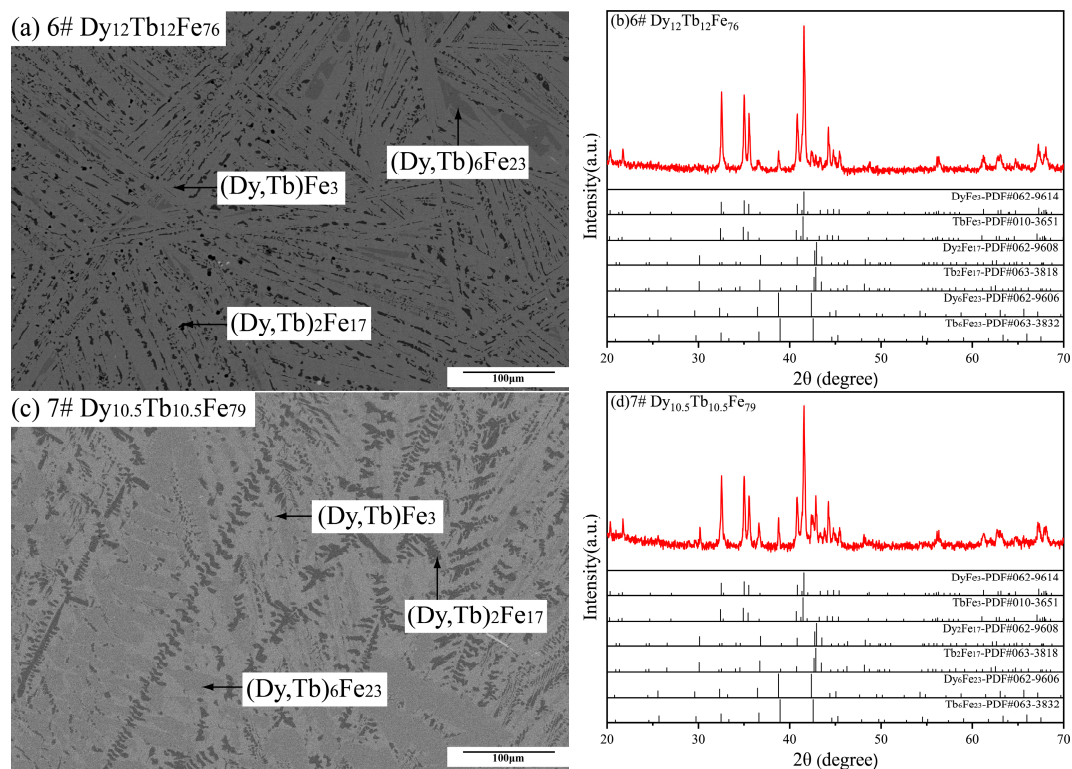


**Figure 5.** Back-scattered electron (BSE) micrographs and XRD patterns of  $\text{Dy}_{12}\text{Tb}_{12}\text{Fe}_{76}$  and  $\text{Dy}_{10.5}\text{Tb}_{10.5}\text{Fe}_{79}$  as-cast alloy samples. (a,b)  $\text{Dy}_{12}\text{Tb}_{12}\text{Fe}_{76}$ , (c,d)  $\text{Dy}_{10.5}\text{Tb}_{10.5}\text{Fe}_{79}$ .

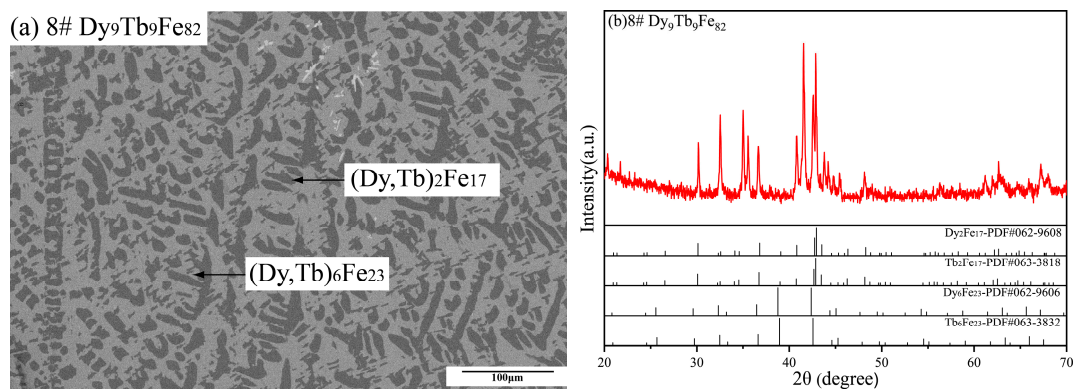


**Figure 6.** (a) Back-scattered electron (BSE) micrographs and (b) XRD patterns of  $\text{Dy}_9\text{Tb}_9\text{Fe}_{82}$  as-cast alloy sample.

Based on the experimental results of eight Dy-Tb-Fe alloy samples with the compositions of  $x_{\text{Dy}} : x_{\text{Tb}} = 1 : 1$  determined by SEM-EDS and XRD, it was noted that the stable ternary intermetallic compound was not determined in this work. In addition, the EDS results measured in Table 1 illustrate that the solubilities of Dy in  $\text{TbFe}_2$ ,  $\text{TbFe}_3$ ,  $\text{Tb}_6\text{Fe}_{23}$  and  $\text{Tb}_2\text{Fe}_{17}$  as well as those of Tb in  $\text{DyFe}_2$ ,  $\text{DyFe}_3$ ,  $\text{Dy}_6\text{Fe}_{23}$  and  $\text{Dy}_2\text{Fe}_{17}$  are different. This indicates that  $(\text{Dy}, \text{Tb})\text{Fe}_2$ ,  $(\text{Dy}, \text{Tb})\text{Fe}_3$ ,  $(\text{Dy}, \text{Tb})_6\text{Fe}_{23}$  and  $(\text{Dy}, \text{Tb})_2\text{Fe}_{17}$  all form continuous solid solution phase in the Dy-Tb-Fe system, which was also reported by Westwood et al. [37].

## 5.2. Phase Transition

Figure 7 shows the thermal analysis curve of Dy-Tb-Fe alloy samples in this work. Based on the thermal analysis results, the transition temperatures of Dy-Tb-Fe alloy samples

were analyzed, and the results are listed in Table 1. In Figure 7a, the thermal curve of the  $\text{Dy}_{42.5}\text{Tb}_{42.5}\text{Fe}_{15}$  alloy sample displays three peaks at 1030 K, 1057 K and 1435 K. Combined with Figure 2a, the peaks at 1030 K and 1057 K are generated due to the formation of the hcp (Dy, Tb) phase and the (Dy, Tb)  $\text{Fe}_2$  phase, while the third peak at 1435 K is corresponding to the formation of the hcp (Dy, Tb) phase as the primary phase. The thermal curve of the  $\text{Dy}_{25}\text{Tb}_{25}\text{Fe}_{50}$  alloy sample in Figure 7b presents three signal peaks at 1121 K, 1131 K and 1459 K, respectively, which correspond to the formation of the (Dy, Tb)  $\text{Fe}_2$  and the hcp (Dy, Tb) phase. Nevertheless, the thermal curve of the  $\text{Dy}_{20}\text{Tb}_{20}\text{Fe}_{60}$  alloy sample in Figure 7c shows only one endothermic peak at 1490 K, corresponding to the formation of (Dy, Tb)  $\text{Fe}_2$ , although the solidification microstructures of both  $\text{Dy}_{25}\text{Tb}_{25}\text{Fe}_{50}$  and  $\text{Dy}_{20}\text{Tb}_{20}\text{Fe}_{60}$  alloy samples contain the (Dy, Tb)  $\text{Fe}_2$  and hcp (Dy, Tb) phases. In Figure 7d,e, the thermal analysis curves of  $\text{Dy}_{15}\text{Tb}_{15}\text{Fe}_{70}$  and  $\text{Dy}_{13.5}\text{Tb}_{13.5}\text{Fe}_{73}$  alloy samples indicate two peaks at 1494/1475 K and 1501/1505 K, corresponding to the formation of (Dy, Tb)  $\text{Fe}_2$  and (Dy, Tb)  $\text{Fe}_3$ . Similarly, the thermal analysis curve of the  $\text{Dy}_{12}\text{Tb}_{12}\text{Fe}_{76}$  alloy sample in Figure 7f indicates three signal peaks at 1482 K, 1495 K and 1555 K, corresponding to the formation of (Dy, Tb)  $\text{Fe}_3$ , (Dy, Tb)<sub>6</sub>  $\text{Fe}_{23}$  and (Dy, Tb)<sub>2</sub>  $\text{Fe}_{17}$ . However, two peaks at 1497 K and 1562 K were observed in the DTA results of the  $\text{Dy}_{10.5}\text{Tb}_{10.5}\text{Fe}_{79}$  alloy sample in Figure 7g, although the solidification microstructures of both  $\text{Dy}_{12}\text{Tb}_{12}\text{Fe}_{76}$  and  $\text{Dy}_{10.5}\text{Tb}_{10.5}\text{Fe}_{79}$  alloy samples consist of (Dy, Tb)  $\text{Fe}_3$ , (Dy, Tb)<sub>6</sub>  $\text{Fe}_{23}$  and (Dy, Tb)<sub>2</sub>  $\text{Fe}_{17}$ . As shown in Figure 7h, two endothermic peaks at 1523 K and 1560 K were observed in the  $\text{Dy}_9\text{Tb}_9\text{Fe}_{82}$  alloy sample, which correspond to the formation of (Dy, Tb)<sub>6</sub>  $\text{Fe}_{23}$  and (Dy, Tb)<sub>2</sub>  $\text{Fe}_{17}$ . In addition, the oxidation peaks due to the easy oxidation of Dy-Tb-Fe alloy samples at high temperatures were also observed in Figure 7f,h.

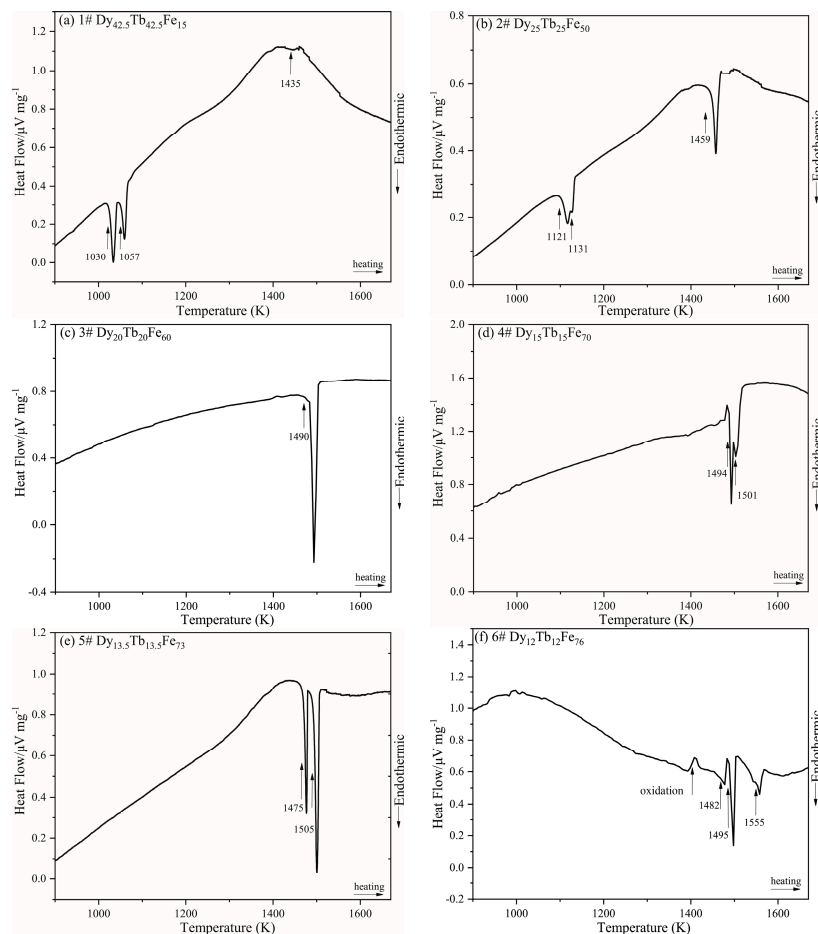
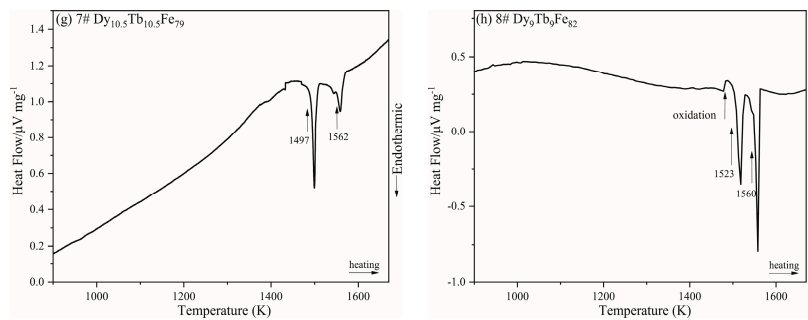


Figure 7. Cont.



**Figure 7.** Thermal analysis curves of Dy-Tb-Fe alloy samples measured by DTA at heating rate of 20 K/min. (a) Dy<sub>42.5</sub>Tb<sub>42.5</sub>Fe<sub>15</sub>, (b) Dy<sub>25</sub>Tb<sub>25</sub>Fe<sub>50</sub>, (c) Dy<sub>20</sub>Tb<sub>20</sub>Fe<sub>60</sub>, (d) Dy<sub>15</sub>Tb<sub>15</sub>Fe<sub>70</sub>, (e) Dy<sub>13.5</sub>Tb<sub>13.5</sub>Fe<sub>73</sub>, (f) Dy<sub>12</sub>Tb<sub>12</sub>Fe<sub>76</sub>, (g) Dy<sub>10.5</sub>Tb<sub>10.5</sub>Fe<sub>79</sub>, (h) Dy<sub>9</sub>Tb<sub>9</sub>Fe<sub>82</sub>.

### 5.3. Thermodynamic Calculation

Based on the experimental data determined in this work and reported by Westwood et al. [37] as well as previous evaluations of Dy-Fe, Tb-Fe, and Tb-Dy systems, the Dy-Tb-Fe system was calculated. The thermodynamic parameters of the Dy-Tb-Fe system obtained are listed in Table 2.

**Table 2.** Thermodynamic parameters of the Dy-Tb-Fe system.

Phase	Thermodynamic Parameters	Reference
Liquid	${}^0L_{Fe,Dy}^{Liquid} = -32,524.791 + 10.7T$	[24]
	${}^1L_{Fe,Dy}^{Liquid} = 14,150.219 - 1.17T$	[24]
	${}^2L_{Fe,Dy}^{Liquid} = 422.595 - 8.2T$	[24]
	${}^0L_{Fe,Tb}^{Liquid} = -20,115.512 - 3.2T$	[24]
	${}^1L_{Fe,Tb}^{Liquid} = -3332.5193 - 11.1T$	[24]
	${}^2L_{Fe,Tb}^{Liquid} = 660.3 - 8.1T$	[24]
	${}^0L_{Dy,Tb,Fe}^{Liquid} = 6000$	This work
bcc ( $\alpha$ -Fe, $\delta$ -Fe, $\beta$ -Dy, $\beta$ -Tb)	${}^0L_{Fe,Dy}^{bcc} = 38,000$	[24]
	${}^0L_{Fe,Tb}^{bcc} = 58,000$	[24]
fcc ( $\gamma$ -Fe)	${}^0L_{Fe,Dy}^{fcc} = 38,000$	[24]
	${}^0G_{Dy}^{fcc} = {}^0G_{Dy}^{hcp} + 5000$	[24]
	${}^0L_{Fe,Tb}^{fcc} = 75,000$	[24]
	${}^0G_{Tb}^{fcc} = {}^0G_{Tb}^{hcp} + 5000$	[24]
hcp ( $\alpha$ -Dy, $\alpha$ -Tb)	${}^0L_{Fe,Dy}^{hcp} = 100,000$	[24]
	${}^0L_{Fe,Tb}^{hcp} = 150,000$	[24]
Fe <sub>17</sub> RE <sub>2</sub> (Fe <sub>17</sub> Dy <sub>2</sub> , Fe <sub>17</sub> Tb <sub>2</sub> )	$G_m^{Fe_{17}Dy_2} = -12,882 + 3.477T + 0.1053{}^0G_{Dy}^{hcp} + 0.8947{}^0G_{Fe}^{bcc}$	[24]
	$T_c^{Fe_{17}Dy_2} = 371, \beta_0^{Fe_{17}Dy_2} = 0.161$	[24]
	$G_m^{Fe_{17}Tb_2} = -10,343 + 1.668T + 0.1053{}^0G_{Tb}^{hcp} + 0.8947{}^0G_{Fe}^{bcc}$	[24]
	$T_c^{Fe_{17}Tb_2} = 408, \beta_0^{Fe_{17}Tb_2} = 0.167$	[24]
	${}^0L_{Dy,Tb,Fe}^{Fe_{17}RE_2} = -2000$	This work
Fe <sub>23</sub> RE <sub>6</sub> (Fe <sub>23</sub> Dy <sub>6</sub> , Fe <sub>23</sub> Tb <sub>6</sub> )	$G_m^{Fe_{23}Dy_6} = -15,700 + 3.909T + 0.2069{}^0G_{Dy}^{hcp} + 0.7931{}^0G_{Fe}^{bcc}$	[24]
	$T_c^{Fe_{23}Dy_6} = 534, \beta_0^{Fe_{23}Dy_6} = 0.1$	[24]
	$G_m^{Fe_{23}Tb_6} = -12,501 + 0.355T + 0.2069{}^0G_{Tb}^{hcp} + 0.7931{}^0G_{Fe}^{bcc}$	[24]
	$T_c^{Fe_{23}Tb_6} = 574, \beta_0^{Fe_{23}Tb_6} = 0.01$	[24]
	${}^0L_{Dy,Tb,Fe}^{Fe_{23}RE_6} = -2000$	This work

Table 2. Cont.

Phase	Thermodynamic Parameters	Reference
Fe <sub>3</sub> RE (Fe <sub>3</sub> Dy, Fe <sub>3</sub> Tb)	$G_m^{Fe_3Dy} = -15,506 + 3.101T + 0.25^0 G_{Dy}^{hcp} + 0.75^0 G_{Fe}^{bcc}$	[24]
	$T_c^{Fe_3Dy} = 606, \beta_0^{Fe_3Dy} = 0.493$	[24]
	$G_m^{Fe_3Tb} = -12,008 - 0.277T + 0.25^0 G_{Tb}^{hcp} + 0.75^0 G_{Fe}^{bcc}$	[24]
	$T_c^{Fe_3Tb} = 652, \beta_0^{Fe_3Tb} = 0.426$ ${}^0L_{Dy,Tb:Fe}^{Fe_3RE} = -3000$	[24] This work
Fe <sub>2</sub> RE (Fe <sub>2</sub> Dy, Fe <sub>2</sub> Tb)	$G_m^{Fe_2Dy} = -17,860 - 5.419T - 0.00672T^2 + 3R\left\{105 + T \ln\left[1 - \exp\left(-\frac{210}{T}\right)\right]\right\}$	[24]
	$T_c^{Fe_2Dy} = 635, \beta_0^{Fe_2Dy} = 0.89$	[24]
	$G_m^{Fe_2Tb} = -14,540 - 4.332T - 0.0074T^2 + 3R\left\{\frac{185}{2} + T \ln\left[1 - \exp\left(-\frac{185}{T}\right)\right]\right\}$	[24]
	$T_c^{Fe_2Tb} = 704, \beta_0^{Fe_2Tb} = 0.762$	[24]
	${}^0L_{Dy,Tb:Fe}^{Fe_2RE} = -4000$	This work

Figure 8 shows the calculated liquidus projection of the Dy-Tb-Fe system. It was found that no invariant reactions are existent in this ternary system. The calculated liquidus projection agrees with the experimental results of the primary phase determined in the experiment. Figure 9 shows the vertical sections of Tb<sub>0.50</sub>Dy<sub>0.50</sub>-Fe and Tb<sub>0.27</sub>Dy<sub>0.73</sub>-Fe calculated based on the experimental data determined in this work and reported by Westwood et al. [37]. The calculation results differ slightly from the experimental results and are still accepted within the experimental errors considering the oxidation of Dy-Tb-Fe alloy samples in the thermal analysis measurements at high temperature.

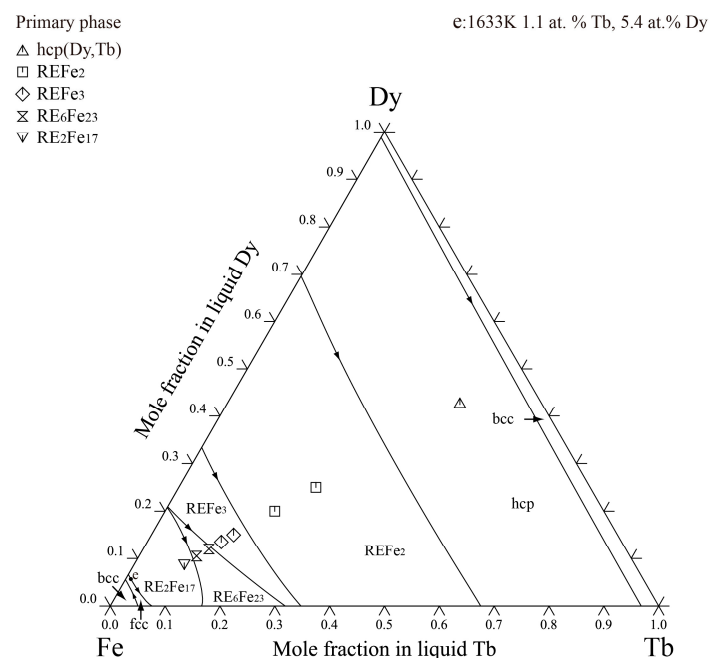
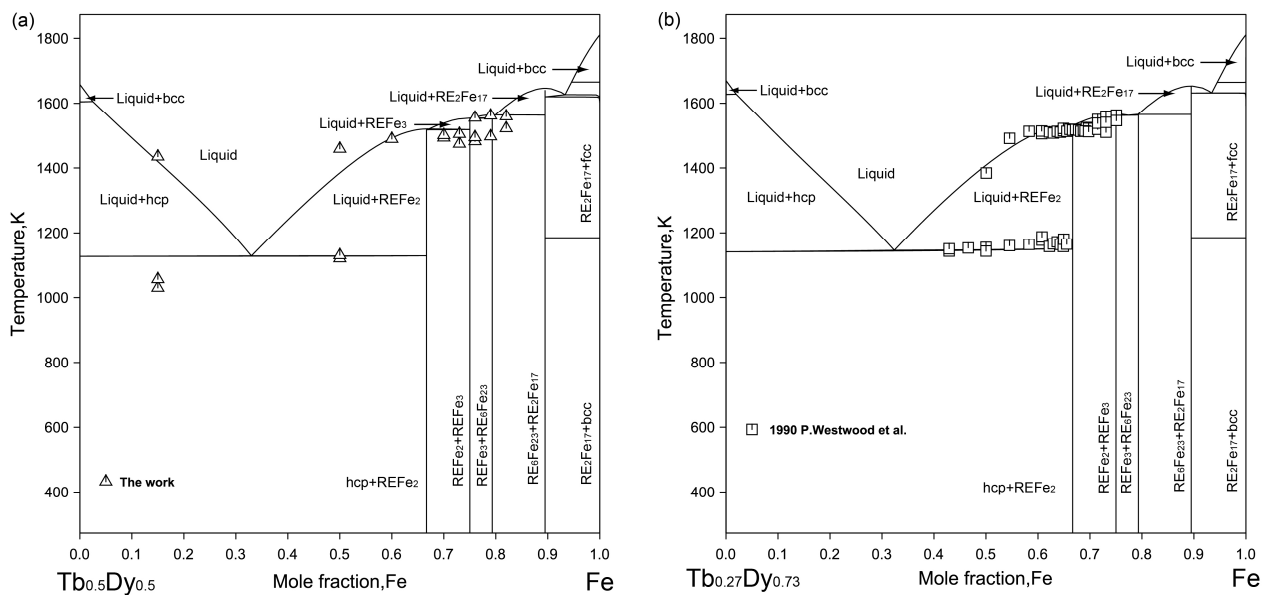
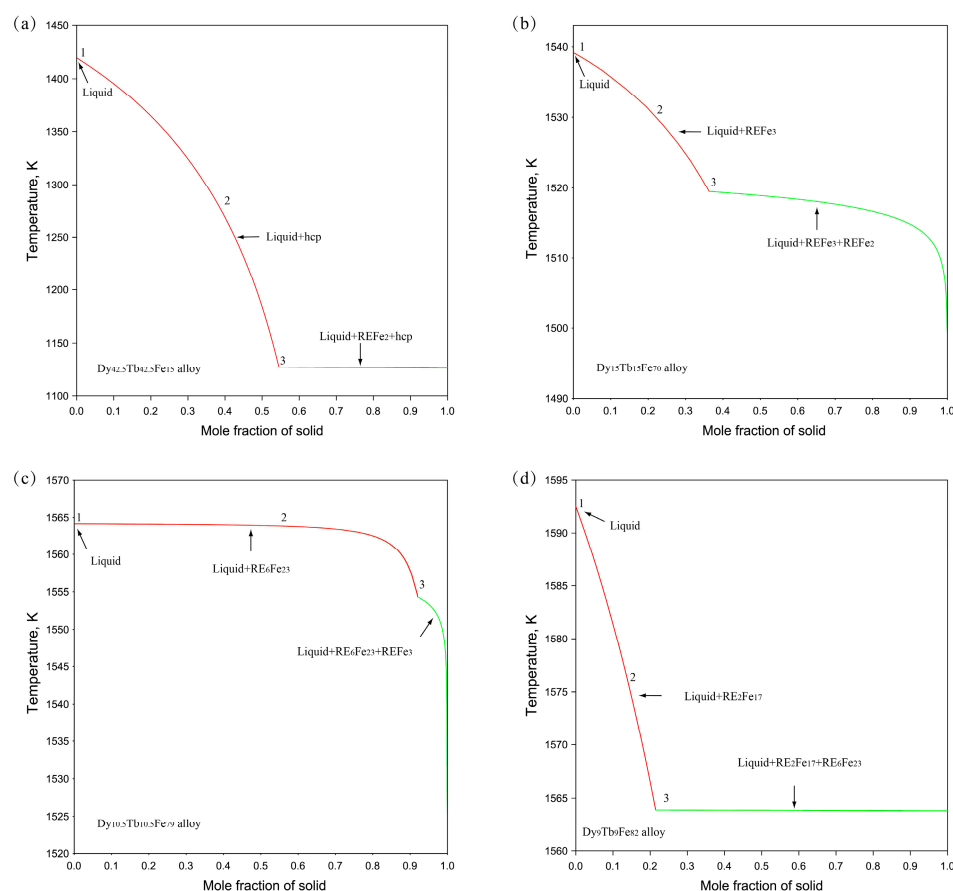


Figure 8. The calculated liquidus projection of the Dy-Tb-Fe system with the experimental results determined in this work.



**Figure 9.** The calculated vertical sections under the different composition conditions with the experimental data measured in this work and reported by Westwood et al. [37]. (a)  $x_{Dy} : x_{Tb} = 1 : 1$ , (b)  $x_{Dy} : x_{Tb} = 0.73 : 0.27$ .

In order to gain a deeper understanding of the phase transformation of Dy-Tb-Fe alloy samples during the non-equilibrium solidification process, the thermodynamic parameters of the Dy-Tb-Fe system obtained in this work were employed to simulate the solidification process of the as-cast alloy samples using the Gulliver–Scheil model. Figure 10 displays the solidification process of four alloy samples ( $Dy_{42.5}Tb_{42.5}Fe_{15}$ ,  $Dy_{15}Tb_{15}Fe_{70}$ ,  $Dy_{10.5}Tb_{10.5}Fe_{79}$ , and  $Dy_9Tb_9Fe_{82}$ ) simulated using the Gulliver–Scheil module. The simulated solidification path of the  $Dy_{42.5}Tb_{42.5}Fe_{15}$  alloy sample in Figure 10a is as follows:  $L \rightarrow hcp(Dy, Tb) + L \rightarrow hcp(Dy, Tb) + L + (Dy, Tb)Fe_2$ . The calculated results show that the solidification structure of the  $Dy_{42.5}Tb_{42.5}Fe_{15}$  alloy sample consists of a hcp (Dy, Tb) phase and (Dy, Tb)  $Fe_2$ , which is consistent with the microstructure observation results shown in Figure 2a. Figure 10b shows the simulated solidification path of the  $Dy_{15}Tb_{15}Fe_{70}$  alloy sample:  $L \rightarrow (Dy, Tb)Fe_3 + L \rightarrow (Dy, Tb)Fe_3 + L + (Dy, Tb)Fe_2$ . It indicates that the microstructure of the  $Dy_{15}Tb_{15}Fe_{70}$  alloy sample consists of (Dy, Tb)  $Fe_3$  and (Dy, Tb)  $Fe_2$ . The simulation results are the same as the SEM results shown in Figure 4a. Similarly, Figure 10c shows the simulated solidification path of the  $Dy_{10.5}Tb_{10.5}Fe_{79}$  alloy sample:  $L \rightarrow L + (Dy, Tb)_6Fe_{23} \rightarrow L + (Dy, Tb)_6Fe_{23} + (Dy, Tb)Fe_3$ , while the simulated solidification path of the  $Dy_9Tb_9Fe_{82}$  alloy sample in Figure 10d is as follows:  $L \rightarrow L + (Dy, Tb)_2Fe_{17} \rightarrow L + (Dy, Tb)_2Fe_{17} + (Dy, Tb)_6Fe_{23}$ , which is consistent with the microstructure observation results shown in Figures 5c and 6a. This indicates that reliable thermodynamic data of the Dy-Tb-Fe system was obtained in this work, which can be employed to reproduce well the solidification processes of Dy-Tb-Fe alloy samples using the Gulliver–Scheil module.



**Figure 10.** Calculated Scheil–Gulliver solidification curves of the representative Dy-Tb-Fe as-cast alloy samples. (a)  $Dy_{42.5}Tb_{42.5}Fe_{15}$ , (b)  $Dy_{15}Tb_{15}Fe_{70}$ , (c)  $Dy_{10.5}Tb_{10.5}Fe_{79}$ , (d)  $Dy_9Tb_9Fe_{82}$ .

## 6. Conclusions

This work investigates the solidification behavior of the Dy-Tb-Fe system using experimental measurements and thermodynamic calculations. The conclusions drawn are as follows:

1. The phase transition temperatures and phase compositions of eight Dy-Tb-Fe alloy samples were determined. Based on the experimental results determined in this work and reported in the literature, the thermodynamic calculation of the Dy-Tb-Fe system was performed using the CALPHAD method. The calculated vertical section and liquidus projection are consistent with the experimental results.
2. The solidification behaviors of several Dy-Tb-Fe alloy samples were simulated by using the Gulliver–Scheil non-equilibrium model with the obtained thermodynamic parameters. The simulation results were compared with the solidification structure of the experimental samples, and they were in good agreement with the experimental results. This means that the thermodynamic parameters of the Dy-Tb-Fe system optimized in this work are reliable and will provide reference for the microstructure design of high-performance Nd-Dy-Tb-Fe-B magnets.

**Author Contributions:** C.T. and J.W. conceived and designed the calculations and the experiments; C.T. and Q.W. performed the calculations and the experiments; W.C., X.L. and Y.B. analyzed the data; C.T. and J.W. wrote the paper. All authors have read and agreed to the published version of the manuscript.

**Funding:** This research was funded by Guangxi Natural Science Foundation (2020GXNSFFA297004), National Natural Science Foundation of China (51971069, 51761008), Guangxi Key Laboratory of In-

formation Materials (211007-Z) and Engineering Research Center of Electronic Information Materials and Devices (EIMD-AA202004), Guilin University of Electronic Technology, China.

**Institutional Review Board Statement:** Not applicable.

**Informed Consent Statement:** Not applicable.

**Data Availability Statement:** All the data that support the findings of this study are included within the article.

**Acknowledgments:** The authors thank the support from the foundation for Guangxi Bagui scholars.

**Conflicts of Interest:** The authors declare no conflict of interest.

## References

1. Poudyal, N.; Liu, J.P. Advances in nanostructured permanent magnets research. *J. Phys. D Appl. Phys.* **2012**, *46*, 043001. [[CrossRef](#)]
2. Coey, J.M.D. Perspective and prospects for rare earth permanent magnets. *Engineering* **2020**, *6*, 119–131. [[CrossRef](#)]
3. Nakamura, H. The current and future status of rare earth permanent magnets. *Scr. Mater.* **2018**, *154*, 273–276. [[CrossRef](#)]
4. Gutfleisch, O.; Willard, M.A.; Brück, E.; Chen, C.H.; Sankar, S.G.; Liu, J.P. Magnetic materials and devices for the 21st century: Stronger, lighter, and more energy efficient. *Adv. Mater.* **2011**, *23*, 821–842. [[CrossRef](#)]
5. Sugimoto, S. Current status and recent topics of rare-earth permanent magnets. *J. Phys. D Appl. Phys.* **2011**, *44*, 064001. [[CrossRef](#)]
6. Davies, B.E.; Mottram, R.S.; Harris, I.R. Recent developments in the sintering of NdFeB. *Mater. Chem. Phys.* **2001**, *67*, 272–281. [[CrossRef](#)]
7. Li, W.F.; Ohkubo, T.; Hono, K.; Sagawa, M. The origin of coercivity decrease in fine grained Nd-Fe-B sintered magnets. *J. Magn. Magn. Mater.* **2009**, *321*, 1100–1105. [[CrossRef](#)]
8. Li, J.; Sepehri-Amin, H.; Sasaki, T.; Ohkubo, T.; Hono, K. Most frequently asked questions about the coercivity of Nd-Fe-B permanent magnets. *Sci. Technol. Adv. Mater.* **2021**, *22*, 386–403. [[CrossRef](#)] [[PubMed](#)]
9. Chen, F.; Zhang, T.; Zhao, Y.; Wang, X.; Jiang, C.; Chen, J.; Zhao, W. A novel strategy to design and fabricate Nd-Fe-B magnets. *J. Alloys Compd.* **2021**, *867*, 159102. [[CrossRef](#)]
10. Trench, A.; Sykes, J.P. Rare earth permanent magnets and their place in the future economy. *Engineering* **2020**, *6*, 115–118. [[CrossRef](#)]
11. Löwe, K.; Brombacher, C.; Katter, M.; Gutfleisch, O. Temperature-dependent Dy diffusion processes in Nd-Fe-B permanent magnets. *Acta Mater.* **2015**, *83*, 248–255. [[CrossRef](#)]
12. Pan, M.; Zhang, P.; Li, X.; Ge, H.; Wu, Q.; Jiao, Z.; Liu, T. Effect of Terbium addition on the coercivity of the sintered NdFeB magnets. *J. Rare Earths* **2010**, *28*, 399–402. [[CrossRef](#)]
13. Li, W.; Yang, L.; Zhang, Q.; Xu, C.; Zhu, Q.; Song, Z.; Zheng, B.; Hu, F.; Jiang, J. Effect of the grain boundary Tb/Dy diffused microstructure on the magnetic properties of sintered Nd-Fe-B magnets. *J. Magn. Magn. Mater.* **2020**, *502*, 166491. [[CrossRef](#)]
14. Divinski, S.V.; Bokstein, B.S. Recent advances and unsolved problems of grain boundary diffusion. *Defect Diffus. Forum* **2011**, *1212*, 309–310. [[CrossRef](#)]
15. Chen, F. Recent progress of grain boundary diffusion process of Nd-Fe-B magnets. *J. Magn. Magn. Mater.* **2020**, *514*, 167227. [[CrossRef](#)]
16. Li, W.; Zhang, Q.; Zhu, Q.; Xiao, S.; Xu, C.; Yang, L.; Zheng, B.; Mao, S.; Song, Z. Formation of anti-shell/core structure of heavy rare earth elements (Tb, Dy) in sintered Nd-Fe-B magnet after grain boundary diffusion process. *Scr. Mater.* **2019**, *163*, 40–43. [[CrossRef](#)]
17. Liu, Z.; He, J.; Ramanujan, R.V. Significant progress of grain boundary diffusion process for cost-effective rare earth permanent magnets: A review. *Mater. Des.* **2021**, *209*, 110004. [[CrossRef](#)]
18. Luo, Q.; Guo, Y.; Liu, B.; Feng, Y.; Zhang, J.; Li, Q.; Chou, K. Thermodynamics and kinetics of phase transformation in rare earth–magnesium alloys: A critical review. *J. Mater. Sci. Technol.* **2020**, *44*, 171–190. [[CrossRef](#)]
19. Schaffnit, P.; Stallybrass, C.; Konrad, J.; Stein, F.; Weinberg, M. A Scheil–Gulliver model dedicated to the solidification of steel. *Calphad* **2015**, *48*, 184–188. [[CrossRef](#)]
20. Chen, T.L.; Wang, J.; Rong, M.H.; Rao, G.H.; Zhou, H.Y. Experimental investigation and thermodynamic assessment of the Fe-Pr and Fe-Nd binary systems. *Calphad* **2016**, *55*, 270–280. [[CrossRef](#)]
21. Chen, X.L.; Wang, J.; Chen, T.L.; Lin, X.D.; Rong, M.H.; Rao, G.H.; Zhou, H.Y. Thermodynamic reassessment of the Fe-Gd and Fe-Sm binary systems. *Calphad* **2017**, *58*, 151–159. [[CrossRef](#)]
22. Rong, M.H.; Chen, X.L.; Wang, J.; Rao, G.H.; Zhou, H.Y. Thermodynamic re-assessment of the Fe-Dy and Fe-Tb binary systems. *Calphad* **2017**, *59*, 154–163. [[CrossRef](#)]
23. Xu, L.; Wang, J.; Li, S.; Chen, X.L.; Rong, M.H.; Rao, G.H.; Zhou, H.Y. Thermodynamic reassessment of the Fe-Tm and Fe-Ho binary systems. *Calphad* **2019**, *66*, 101646. [[CrossRef](#)]
24. Ye, H.J.; Rong, M.H.; Yao, Q.R.; Wang, J.; Chen, Q.; Rao, G.H.; Zhou, H.Y. Assessment of phase equilibria and thermodynamic properties in the Fe-RE (RE = rare earth metals) binary systems. *J. Mater. Inform.* **2023**, *3*, 14.

25. Li, S.; Rong, M.H.; Xu, L.; Wei, Q.; Wang, J.; Rao, G.H.; Zhou, H.Y. Thermodynamic assessment of the RE-B (RE = Ce, Dy, Lu) binary systems. *Calphad* **2020**, *68*, 101740. [[CrossRef](#)]
26. Wei, Q.; Rong, M.H.; Li, S.; Su, D.; Yao, Q.R.; Wang, J.; Rao, G.H.; Zhou, H.Y. Thermodynamic assessment of the RE-B (RE = Ho, Er, Tm) binary systems. *Calphad* **2020**, *70*, 101796. [[CrossRef](#)]
27. Wei, Q.; Rong, M.H.; Li, S.; Su, D.; Rao, Q.R.; Wang, J.; Chen, Q.; Rao, G.H.; Zhou, H.Y. Thermodynamic calculation of phase equilibria of rare earth metals with boron binary systems. *Int. J. Mater. Res.* **2022**, *113*, 400–418. [[CrossRef](#)]
28. Yang, K.C.; Wang, J.; Yao, Q.R.; Lu, Z.; Rong, M.H.; Zhou, H.Y.; Rao, G.H. Phase diagrams of permanent magnet alloys: Binary rare earth alloy systems. *J. Rare Earths* **2019**, *37*, 1040–1046. [[CrossRef](#)]
29. Su, D.; Yang, K.C.; Rong, M.H.; Liu, P.P.; Yao, Q.R.; Wang, J.; Chen, Q.; Rao, G.H.; Zhou, H.Y. Phase transition and solidification microstructure of Ce-La-Fe and Ce-Nd-Fe alloys: Experimental investigation and thermodynamic calculation. *Calphad* **2023**, *80*, 102506. [[CrossRef](#)]
30. Su, D.; Rong, M.H.; Yang, K.C.; Yao, Q.R.; Wang, J.; Rao, G.H.; Zhou, H.Y. Thermodynamic calculation and solidification behavior of the La-Pr-Fe and Ce-Pr-Fe ternary systems. *Calphad* **2021**, *74*, 102285. [[CrossRef](#)]
31. Chen, T.L.; Wang, J.; Guo, C.P.; Li, C.R.; Du, Z.M.; Rao, G.H.; Zhou, H.Y. Thermodynamic description of the Nd-Fe-B ternary system. *Calphad* **2019**, *66*, 101627. [[CrossRef](#)]
32. Landin, S.; Ågren, J. Thermodynamic assessment of Fe-Tb and Fe-Dy phase diagrams and prediction of Fe-Tb-Dy phase diagram. *J. Alloys Compd.* **1994**, *207*, 449–453. [[CrossRef](#)]
33. Gschneidner, K.A.; Calderwood, F.W. Use of systematics for the evaluation of rare-earth phase diagrams and crystallographic data. *Bull. Alloy Phase Diagr.* **1983**, *4*, 129–131. [[CrossRef](#)]
34. Gschneidner, K.A.; Calderwood, F.W. Intra rare earth binary alloys: Phase relationships, lattice parameters and systematics. *Handb. Phys. Chem. Rare Earths* **1986**, *8*, 1–161. [[CrossRef](#)]
35. Moffatt, W.G. *Binary Phase Diagrams Handbook*; General Electric Comp: Schenectady, NY, USA, 1987.
36. Raghavan, V. Dy-Fe-Tb (dysprosium-iron-terbium). *J. Phase Equilibria Diffus.* **2004**, *25*, 169. [[CrossRef](#)]
37. Westwood, P.; Abell, J.S.; Pitman, K.C. Phase relationships in the Tb-Dy-Fe ternary system. *J. Appl. Phys.* **1990**, *67*, 4998–5000. [[CrossRef](#)]
38. Abell, J.S.; Lord, D.G. Microstructural studies of ternary rare earth-iron alloys. *J. Less Common Met.* **1986**, *126*, 107–112. [[CrossRef](#)]
39. Dinsdale, A.T. SGTE data for pure elements. *Calphad* **1991**, *15*, 317–425. [[CrossRef](#)]
40. Van der Goot, A.S.; Buschow, K.H.J. The dysprosium-iron system: Structural and magnetic properties of dysprosium-iron compounds. *J. Less-Common Met.* **1970**, *21*, 151–157. [[CrossRef](#)]
41. Okamoto, H. Dy-Fe (dysprosium-iron). *J. Phase Equilibria* **1996**, *17*, 80–81. [[CrossRef](#)]
42. Dariel, M.P.; Holthuis, J.T.; Pickus, M.R. The terbium-iron phase diagram. *J. Less-Common Met.* **1976**, *45*, 91–101. [[CrossRef](#)]

**Disclaimer/Publisher’s Note:** The statements, opinions and data contained in all publications are solely those of the individual author(s) and contributor(s) and not of MDPI and/or the editor(s). MDPI and/or the editor(s) disclaim responsibility for any injury to people or property resulting from any ideas, methods, instructions or products referred to in the content.